

Article

Enhancing the Catalytic Activity of Layered Double Hydroxide Supported on Graphene for Lithium–Sulfur Redox Reactions

Junjie Xu ^{1,†}, Rui Tang ^{1,†}, Minghui Liu ¹, Shuai Xie ², Dawei Zhang ¹, Xianghua Kong ^{1,*}, Song Jin ^{2,*}, Hengxing Ji ² and Tierui Zhang ^{3,*}

¹ School of Chemistry and Chemical Engineering, Hefei University of Technology, Hefei 230009, China

² National Laboratory for Physical Sciences at the Microscale, CAS Key Laboratory of Materials for Energy Conversion, Department of Applied Chemistry, University of Science and Technology of China, Hefei 230026, China

³ Key Laboratory of Photochemical Conversion and Optoelectronic Materials, Technical Institute of Physics and Chemistry, Chinese Academy of Sciences, Beijing 100190, China

* Correspondence: kongxh@hfut.edu.cn (X.K.); js199155@ustc.edu.cn (S.J.); tierui@mail.ipc.ac.cn (T.Z.)

† These authors contributed equally to this work.

Abstract: The lithium–sulfur battery is one of the next-generation rechargeable battery candidates due to its high theoretical energy density and low cost. However, the sluggish conversion kinetics of soluble lithium polysulfides into insoluble $\text{Li}_2\text{S}_2/\text{Li}_2\text{S}$ leads to low sulfur utilization, retarded rate responses, and rapid capacity decay. Here, we enhance the sulfur reduction kinetics by designing and synthesizing a lamellar-structured NiFeLDH and reduced graphene oxide (rGO) composite. The assembly of a two-dimensional NiFeLDH with rGO, which has high conductivity and electrocatalytic activity, significantly enhances the electrochemical steps of sulfur reduction. The S@NiFeLDH/rGO cathode delivers an initial discharge capacity of 1014 mAh g^{-1} at 0.2 C and a capacity of 930 mAh g^{-1} after 100 cycles at 0.2 C . Even at a high current density of 1 C , the S@NiFeLDH/rGO could maintain a high capacity of 554 mAh g^{-1} after 400 cycles.

Keywords: layered double hydroxide; graphene; catalyst; lithium–sulfur battery



Citation: Xu, J.; Tang, R.; Liu, M.; Xie, S.; Zhang, D.; Kong, X.; Jin, S.; Ji, H.; Zhang, T. Enhancing the Catalytic Activity of Layered Double Hydroxide Supported on Graphene for Lithium–Sulfur Redox Reactions. *Batteries* **2022**, *8*, 200. <https://doi.org/10.3390/batteries8110200>

Academic Editor: Lin Li

Received: 20 September 2022

Accepted: 24 October 2022

Published: 29 October 2022

Publisher's Note: MDPI stays neutral with regard to jurisdictional claims in published maps and institutional affiliations.



Copyright: © 2022 by the authors. Licensee MDPI, Basel, Switzerland. This article is an open access article distributed under the terms and conditions of the Creative Commons Attribution (CC BY) license (<https://creativecommons.org/licenses/by/4.0/>).

1. Introduction

Elemental sulfur possesses a high specific capacity of 1672 mAh g^{-1} as a cathode material for lithium batteries. The coupling of sulfur and a lithium metal anode offers a high theoretical energy density up to 2600 Wh kg^{-1} and 2800 Wh L^{-1} [1,2]. However, the practical application of lithium–sulfur (Li–S) batteries is still plagued with numerous challenges. For example, the insulating nature of sulfur and the discharge products $\text{Li}_2\text{S}_2/\text{Li}_2\text{S}$ leads to low sulfur utilization [3–6]. In addition, the soluble intermediate lithium polysulfides (LiPSs) in the electrolyte generated during charge/discharge processes cause LiPSs shuttling between the cathode and anode, where they are reduced to insoluble Li_2S and uncontrollable deposition on the lithium metal anode surface [7–11], inducing low coulombic efficiency and irreversible capacity loss.

Considerable efforts have been taken to circumvent the aforementioned problems, which can fall into two categories: physical adsorption and chemical confinement. For instance, the integration of nanostructured carbon materials with sulfur can suppress polysulfide shuttling through pores or interlayer spaces to physically confine LiPSs [12–15]. The chemical entraptments are introduced by the modification of carbon materials by nonmetallic element doping or surface functionalization and the application of polar compounds to enhance the interaction and immobilization of polar LiPSs [16–20]. Although these strategies can mitigate the shuttle effect to a certain extent, these results are still unsatisfactory. Approximately 75% of the theoretical specific capacity of the Li–S battery is contributed by the conversion of soluble Li_2S_4 to solid Li_2S [21], and the slow kinetics leads

to the continued accumulation of soluble LiPSs in the cathode area and the inhomogeneous precipitation of solid reduction products of $\text{Li}_2\text{S}_2/\text{Li}_2\text{S}$ on the cathode surface. The PS shuttling action is made worse by the buildup of soluble LiPSs in electrolytes, and the deposition of these solid products block the Li-ion transport channels and deactivate the sulfur, resulting in low sulfur utilization and even the “sudden death” of the battery. Fundamentally, these issues are caused by the slow and intricate sulfur reduction reaction (SRR), i.e., the sluggish kinetic conversion of LiPSs to insoluble $\text{Li}_2\text{S}_2/\text{Li}_2\text{S}$ [22]. Therefore, how to catalytically accelerate the transformation from LiPSs to final solid-phase products is one of the keys to solving the problems associated with Li–S batteries.

In recent years, catalysts have been used to accelerate the rate of conversion of LiPSs to insoluble products to increase the utilization of sulfur and improve the battery’s lifecycle. In 2014, Prof. Nazar first suggested that Magnéli-phase Ti_4O_7 could induce surface-mediated redox reactions of LiPSs [23]. Since then, nanocatalysts such as Pt [24], metal oxides [25,26], metal sulfides [27], metal phosphides [28,29], and single-atom catalysts [30] have been used as sulfur hosts to promote LiPSs conversion. Layered double-metal hydroxides (LDHs) are unique two-dimensional ionic lamellar materials consisting of layers of positively charged metal hydroxide and interlayer regions of charge-balancing anions [31]. Two metals with a well-defined crystal structure with fixed atom positions are similar to that of single-atom catalysts and have been widely applied, leading to oxygen reduction reaction [32], electrocatalytic water splitting [33], and CO_2 reduction [34] owing to their superior activity. For the sulfur system, the LDHs possess lots of polar hydroxyl groups on the surface, allowing for chemical bonds with polysulfides, and the metal sites exposed in the LDH may offer enough active sites to kinetically improve polysulfide redox processes [35]. In addition, when the sulfur is loaded into the layers, there is enough room to accommodate its significant volumetric expansion. For example, Lou et al. created double-shelled nanocages with cobalt hydroxide as the sulfur host to enhance the electrochemical performance of Li–S batteries [36]; Min et al. synthesized a $\text{TiO}_2@\text{NiCo-LDH}$ compound to load the sulfur and it was shown to deliver excellent electrochemical performance at different temperatures [37]. Despite LDHs being used as enhanced sulfur host materials for Li–S batteries, the application of LDH in batteries is limited due to its poor electrical conductivity.

In this context, we designed a lamellar-structured sulfur electrode with excellent electrochemistry performance for Li–S batteries. LDHs grew *in situ* on the rGO to create its lamellar structure. The LDHs could chemically block and strongly capture the LiPSs, and meanwhile, the utilization of rGO could improve the electrical conductivity of the composite. In addition, symmetric cells, rotating disk electrodes (RDE), and the nucleation of lithium sulfide measurements identified that NiFeLDH/rGO could serve as an electrocatalyst to facilitate SRR catalytic activity. Benefiting from the above merits, the prepared S@NiFeLDH/rGO cathode delivered an excellent discharge capacity of 1014 mAh g^{-1} , with a capacity fading rate of 0.082% per cycle over 100 cycles at 0.2 C.

2. Materials and Methods

2.1. Raw Materials

Graphene oxide (SE3122) was purchased from The Sixth Element (Changzhou) Materials Technology Co., Ltd. Polyvinylidene fluoride (PVDF 99.5 wt%), N-methyl pyrrolidone (NMP 99.5 wt%), and carbon cloth were purchased from Aladdin reagent. The electrolyte (KLD-S01) and lithium sulfide (Li_2S , 99.98 wt%) were purchased from Guangdong Canrd New Energy Technology Co., Ltd. (Shenzhen, China). Other chemicals such as $\text{Ni}(\text{NO}_3)_2 \cdot 6\text{H}_2\text{O}$, $\text{Fe}(\text{NO}_3)_3 \cdot 9\text{H}_2\text{O}$, NaOH , CH_3NO , $\text{N}_2\text{H}_4 \cdot \text{H}_2\text{O}$, and sulfur were purchased from Sinopharm Chemical Reagent Co., Ltd. (China), and all of the reagents were of analytical grade.

2.2. Material Synthesis

First, 45 mg of GO was added into 100 mL 1:1 (in volume) formamide (CH_3NO)/deionized water. Then, 1.2 mM of $\text{Fe}(\text{NO}_3)_3 \cdot 9\text{H}_2\text{O}$ and 0.6 mM of $\text{Ni}(\text{NO}_3)_2 \cdot 6\text{H}_2\text{O}$ were dissolved in

the above suspension followed by adding a certain mass concentration of NaOH solution until the pH of the final solution was about 10. The obtained suspension was centrifuged for 10 min to obtain the sediment, which was washed three times with ethanol and deionized water, respectively. The sediment was then redispersed in deionized water and 100 μL of 80 wt% hydrazine hydrate ($\text{N}_2\text{H}_4 \cdot \text{H}_2\text{O}$). After the mixture was heated in reactor at 80 $^{\circ}\text{C}$ for 1~2 h, the final NiFeLDH/rGO (NFG) was obtained. The preparation procedure for the other samples with different ratios (NFG-n) was the same, except for the added quantities of $\text{Fe}(\text{NO}_3)_3 \cdot 9\text{H}_2\text{O}$ and $\text{Ni}(\text{NO}_3)_3 \cdot 6\text{H}_2\text{O}$.

2.3. Characterization Methods

XRD characterization of the samples was performed with Cu K α radiation on a Phillips X'Pert Pro MPD diffractometer. XPS analysis was performed on a Thermo Scientific ESCALAB 250Xi X-ray photoelectron spectroscopy using an Al K α excitation source. Raman spectroscopy studies were performed on a HORIBA JOBIN YVON laser confocal Raman microscope with a 523 nm laser source. Thermogravimetric analysis (TGA) was performed by Shimadzu TGA-50H (Shimadzu Corporation, Japan) in an air atmosphere from 25 $^{\circ}\text{C}$ to 700 $^{\circ}\text{C}$ in a thermal analyzer. The specific surface area and pore volume were derived from BET. The samples were studied by scanning electron microscopy (FESEM, S-8010, Hitachi). Scanning transmission electron microscopy (STEM) and HRTEM were run at 200 kV on an FEI Talos F200S electron microscope.

2.4. Symmetric Cell Test

In total, 80 wt% NFG-n and 20 wt% PVDF were dissolved in NMP and coated on aluminum foil, and then dried at 50 $^{\circ}\text{C}$ for 24 h to obtain the symmetric cell electrodes. The electrolyte was composed of 0.5 M lithium bis(trifluoromethanesulfon) imide (LiTFSI) and 0.5 M Li_2S_6 dissolved in 1:1 (in volume) 1,3-dioxolane (DOL)/dimethoxyethane (DME) with 2.0 wt% LiNO_3 . The battery was scanned by 10 mV s $^{-1}$ from -1.4 V to 1.4 V.

2.5. Rotating Disk Electrode Test

For this test, 10 μL of NFG-n slurry (made by sonicating 3 mg of NFG-n powder in 1 mL of ethanol and 20 μL of 5 wt% Nafion solution) was coated on a freshly polished glassy carbon electrode (area 0.1256 cm 2) to form a planar electrode. The lithium foil was used as the counter/reference electrode. The NFG-n electrode was used as the working electrode. The linear scanning voltammetric (LSV) was tested at voltages ranging from 3.3 V to 1 V. The scan rate was 20 mV s $^{-1}$.

2.6. Measurement for the Nucleation of Lithium Sulfide

Here, 80 wt% NFG-n and 20 wt% PVDF were dissolved in NMP and coated on aluminum foil, and then dried at 50 $^{\circ}\text{C}$ for 24 h to obtain the cathode. A lithium foil was used as the anode. The tetraglyme with 0.5 M Li_2S_8 was used as the electrolyte. The cell was galvanostatically discharged to 2.06 V at 0.05 C and then potentiostatically discharged at 2.05 V until the current was less than 0.01 mA.

2.7. Electrochemical Measurements

The S@NFG-n composites were created by combining NFG-n and sulfur powder in a 4:1 weight ratio. After that, the mixture was heated for 10 h at 155 $^{\circ}\text{C}$. The S@NFG-n electrode was prepared by mixing 75 wt% S@NFG-n composite, 15 wt% Ketjen black, and 10 wt% PVDF to obtain a slurry, which was then coated on carbon cloth current collector or aluminum foil. After drying at 50 $^{\circ}\text{C}$ for 24 h, the S@NFG-n electrodes were obtained. The electrodes were punched into circular disks with diameters of 10 mm. The areal loading density of the sulfur is around 1.5–2 mg cm $^{-2}$ based on the mass of the sulfur divided by the projected area of the electrode. The mass S loading, rather than the areal S loading, is calculated by the weight of all cathodes including the current collector, S@NFG-n, Ketjen black, and PVDF. A rough calculation results in a 13 wt% sulfur content in the electrode if

we use 75 wt% sulfur in the S@NFG-n composite and 75 wt% composite in the mixed slurry that is deposited on a carbon cloth (12 mg cm^{-2}). Since the S@NFG-n electrode was coated on the carbon cloth current collector, the thickness of the electrode was around $300 \mu\text{m}$, corresponding to the thickness of the carbon cloth. The electrolyte was composed of 1.0 M LiTFSI dissolved in DOL and DME (1:1 by volume) with 2 wt% LiNO₃. Then, 2025-coin cells were adapted, which consisted of a cathode, a piece of Li anode (with a diameter of 14 mm), and a PP membrane (with a diameter of 19 mm). The electrolyte/sulfur (E/S) ratio was controlled to be $\sim 15 \mu\text{L mg}^{-1}$. The coin cells were tested on a LANDTE system (CT2011A) in the voltage range of 1.7~2.7 V.

3. Results and Discussion

The NiFeLDH has a strong LiPSs capture capability and could serve as an active site for sulfur reduction reaction. However, the inferior electrical conductivity of LDH impeded the electrochemical performance of the Li–S battery. Graphene, as a sp₂-hybridized carbon material, possessed excellent electric conductivity. Therefore, to combine the advantages of both LDH and graphene, we synthesized the lamellar structure of NiFeLDH/rGO using an *in situ* growth method. On account of the 2D structure of NiFeLDH, the LDH could assemble with the graphene matrix via π – π interactions. To balance the catalytic activity and conductivity of the NiFeLDH/rGO composite, we synthesized three sets of NiFeLDH/rGO with different mass ratios. The mass ratio of rGO to LDH was revealed by thermogravimetric analysis (TGA, Figures S1 and 1a). As shown in Figure S1, the pure NiFeLDH displayed two mass-loss steps. The first step was from 30 °C to 150 °C on account of the evaporation of water molecules in interlayer. The second step was from 150 °C to 300 °C, which can be attributed to the dehydroxylation of the LDH. For the pure rGO, one conspicuous weight-loss step was observed at 300–700 °C due to the oxidation of carbons. Thus, the TGA curve showed three stages of significant weight loss after heating the NiFeLDH/rGO composite in air at 700 °C. From the above results, we can calculate the weight percentage of rGO and NiFeLDH based on the weight loss in different temperature intervals. the mass percent of rGO in NFG-30, NFG-5 and NFG-1 are 3%, 17%, and 50%, respectively. Thus, the mass ratios of LDH to rGO were around 30:1, 5:1, and 1:1; we named them NFG-30, NFG-5, and NFG-1, respectively. The X-ray diffraction (XRD) pattern of the three samples contained peaks at 11.4°, 22.8°, 34.2°, and 60.3° that can be assigned to NiFeLDH (Figure 1b) [38]. In addition, the broadened peak at 22° compared to the pristine NiFeLDH was attributed to the overlap between the (002) crystalline facet of rGO and the (006) crystalline facet of LDH. It could be seen that the peak at this position became wider as the ratio of rGO increased. In Figure 1c, Raman spectroscopy demonstrated that all three samples contained two intense peaks located at 1340 cm^{-1} and 1594 cm^{-1} , which were contributed to the D and G bands of graphene, respectively. The D/G values of the three samples were around 1.1, indicating the same degree of graphitization and confirming the presence of rGO in the three NiFeLDH/rGO composites. The surface chemical states of NiFeLDH/rGO and the interactions among rGO and LDH were analyzed by XPS measurement (Figure 1d–f). In the Ni 2p XPS spectra of NFG-5, two major peaks were observed at 873.5 eV and 855.7 eV, which were assigned to the Ni 2p_{1/2} and Ni 2p_{3/2}, respectively, indicating the presence of Ni²⁺ [39]. The peaks of Fe 2p located at 725.1 and 712.2 eV were respectively attributable to Fe 2p_{1/2} and Fe 2p_{3/2}. The refinement of the characteristic peaks of Fe at 711.6 and 714.6 eV demonstrated the presence of Fe in the form of Fe³⁺ cations and Fe^{III}–OH [40]. In addition, oxygen atoms doped into the graphene lattice were present the form of -CH₂-C-, -CH₂-O-, and -C(O)O-, as indicated in the O 1s XPS spectra. The presence of oxygen-containing groups favored the enhancement of the electrostatic interaction between rGO and LDH. The XPS patterns of C 1s, Ni 2p, and Fe 2p in the NFG-30 and NFG-1 samples are shown in Figure S2. The valence states of the metals in NFG-30 and NFG-1 were almost unchanged in comparison with NFG-5. The morphology of NiFeLDH was characterized by transmission electron microscopy (TEM). As shown in Figure S3, only some black spots were observed on the

rGO surface due to the low content of LDH in the NiFeLDH/rGO composite when the mass ratio of LDH to rGO was 1:1. When the mass ratio of LDH to rGO increased to 5:1, the NiFeLDH/rGO composite exhibited a highly random porous architecture, which was composed of NiFeLDH nanoflakes. The NiFeLDH tended to form an agglomerate in NFG-30 when the mass ratio of LDH to rGO increased from 5:1 to 30:1, and we are unable to see the sheet-like morphology of the graphene.

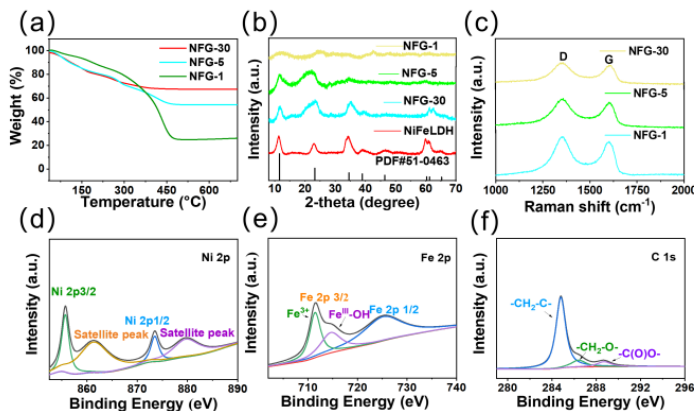


Figure 1. (a) TGA curves of NFG-1, NFG-5, and NFG-30, (b) XRD patterns of NFG-1, NFG-5, NFG-30, and NiFeLDH, and (c) Raman spectra of NFG-1, NFG-5, and NFG-30, respectively. High resolution XPS (d) Ni 2p, (e) Fe 2p, and (f) C 1s of NFG-5.

Similar to previous studies [41], S-loaded NiFeLDH/rGO (S@NFG-1, S@NFG-5, and S@NFG-30) were obtained through a melt-diffusion process to impregnate elemental S in the NiFeLDH/ rGO host. From the TGA curve in Figure 2a, the mass ratio of sulfur was ~75 wt% in three S@NiFeLDH/rGO composites. The morphologies of three S@NiFeLDH/rGO composites were related to the of S, Ni, and Fe element mappings, demonstrating the composite components' consistent chemical makeup (Figure 2b–d). In the following, we measured the electrochemical of S@NiFeLDH/rGO composite based on the S loading of 75 wt%. Due to the low stability of the sulfur particles under electron beams, it is a challenge to ascertain whether the sulfur is inside the layered LDH at the nanoscale using TEM images. The BET measurements show that the encapsulation of sulfur particles reduces the specific surface area from $69.1 \text{ m}^2 \text{ g}^{-1}$ for the NFG-5 to $38.9 \text{ m}^2 \text{ g}^{-1}$ for the S@NFG-5, as well as decreasing the pore volume from $0.25 \text{ to } 0.07 \text{ cm}^3 \text{ g}^{-1}$, demonstrating the successful infiltration of sulfur inside the NFG-5 (Figure S4).

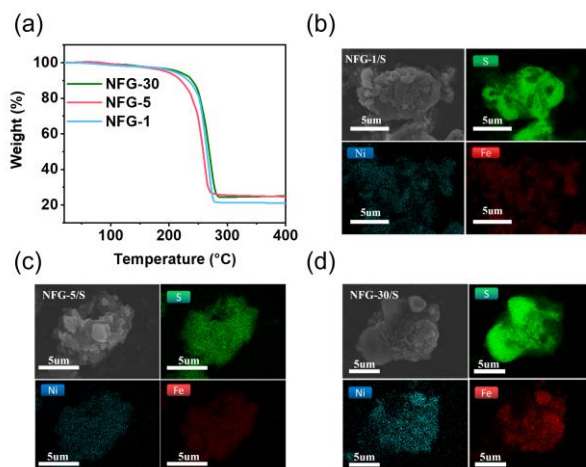


Figure 2. (a) TG curves of S@NFG-30, S@NFG-5, and S@NFG-1. Elemental mapping images of (b) S@NFG-1, (c) S@NFG-5, and (d) S@NFG-30, respectively.

To investigate the electrocatalytic activities of the as-synthesized NiFeLDH/rGO support on the electrochemical conversion of LiPSs, we used two identical electrodes to assemble symmetric cells to test the cyclic voltammetry (CV) (Figure 3a). Here, 0.5 M Li_2S_6 electrolyte was dissolved in the electrolyte as the active sulfur species. The obtained CV curve of NFG-5 presented two pairs of reversible redox peaks, labeled A (-0.49 V), B (-0.51 V), C (0.24 V), and D (0.62 V). Peak A arose from the reduction of S_8 to Li_2S_6 , and peak B was attributed to the conversion of Li_2S_6 to Li_2S . When NFG-5 was used as the electrode of the symmetric cell, NFG-5 showed the highest peak current density of 6.88 mA mg^{-1} and the lowest peak voltage of 0.62 V compared to NFG-1 and NFG-30 (Figure 3b), indicating the fastest conversion reaction rate of LiPSs.

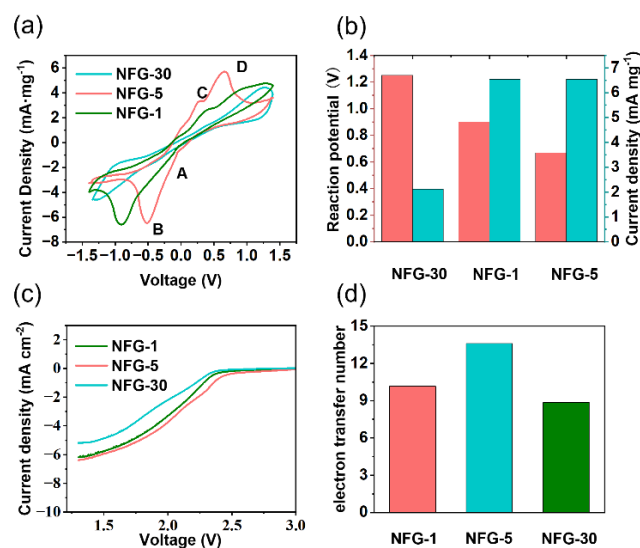


Figure 3. (a) CVs of symmetric cells with NFG-1, NFG-5, and NFG-30 electrodes. (b) Peak D's potentials and current densities. (c) NiFeLDH/rGO linear sweep voltammetry curves in the direction of SRR. (d) An electron transfer n number comparison among NFG-30, NFG-5, and NFG-1 electrodes.

Due to the short reaction time of seconds in the CV experiments, the complete conversion of Li_2S_6 to Li_2S cannot be accomplished. Moreover, in the CV of symmetric cells, the conversion of Li_2S_6 to other lower-order polysulfides such as Li_2S_4 will also contribute to the peak current that cannot be ignored. Under this condition, the CV curves of symmetric cells cannot completely unravel the liquid–solid (Li_2S_6 – Li_2S) conversion. To further investigate the reduction kinetics of the liquid–solid reaction from polysulfides to Li_2S , the potentiostatic nucleation of Li_2S is conducted. During the test, 0.5 M Li_2S_8 electrolyte was dissolved in tetraglyme solvent. The cells were galvanostatically discharged to 2.06 V at 0.05 C for the full reduction of Li_2S_8 to Li_2S_4 , and then discharged potentiostatically at 2.05 V until the current was less than $10 \mu\text{A}$ to further form the Li_2S sediment. The integral area of the curve that was plotted using Faraday's law can be used to calculate the nucleation capacity of Li_2S . As shown in Figure S5, the capacity of Li_2S precipitation on NFG-5 (81 mAh g^{-1}) was better than NFG-1 (66 mAh g^{-1}) and NFG-30 (53 mAh g^{-1}). Furthermore, the current peak of NFG-5 occurred earlier than those of NFG-1 and NFG-30, which indicated the reduced energy barrier of Li_2S nucleation and enhanced electrochemical reaction kinetics on NFG-5.

Since the SRR are multi-electron reactions, we combined linear sweep voltammetry (LSV) with rotating disk electrode (RDE) testing to investigate the redox kinetic behavior of NiFeLDH for S reduction. Figures 3c and S6 show the LSV curves of NFG-30, NFG-5, and NFG-1 deposition. The LSV curves exhibited similar features to the ORR, such as an onset potential, half-wave potential $E_{1/2}$, and diffusion-limited current density j_d . The $E_{1/2}$ of NFG-5 was 2.045 V , which was higher than that of NFG-30 (1.951 V) and NFG-1 (1.883 V), suggesting an overall lower overpotential. The diffusion-limited current density

of NFG-5 was 7.4 mA cm^{-2} , which was higher than NFG-1 (7.39 mA cm^{-2}) and NFG-30 (6.17 mA cm^{-2}), indicating considerably higher electrocatalytic activity. To understand the SRR mechanism with the presence of catalysts, the electron transfer numbers in the SRR process were calculated using the j_d according to the Koutecky–Levich (K-L) equation. The K-L equation is calculated as follows:

$$1/j = 1/j_k + 1/j_d \quad (1)$$

$$j_d = 0.2nFAC_0D^{2/3}v^{-1/6}\omega^{1/2} \quad (2)$$

where the experimentally measured current density is denoted as j , the kinetic control current density of the rotating disk is denoted as j_k , the transfer number of electrons for sulfur reduction is denoted as n , the angular velocity is ω , the Faraday constant is denoted as F , the electrode area is denoted as A , D is the diffusion coefficient of the reactant, and v is the kinematic viscosity of the electrolyte [20]. Combining Equations (1) and (2), the K-L equation is expressed as:

$$1/j = 1/j_k + (1/K) \bullet (1/\omega^{1/2}) \quad (3)$$

where $0.2nFAC_0D^{2/3}v^{-1/6}$ is noted as the constant K . Thus, n can be calculated from the slope of the linear plot of $1/j$ against $1/\omega^{1/2}$ (Figure S7). In Figure 3d, the NFG-5 exhibited an electron transfer number of about 13. By contrast, the electron transfer numbers of NFG-1 and NFG-30 can be calculated as 11.1 and 8.7, respectively. The larger electron transfer number indicated a better promotion of redox reaction kinetics of sulfur conversion.

We also examined the total performance of the NiFeLDH/rGO cathodes in Li–S coin cells to evaluate the electrocatalysts' effect on the performance of the entire cell. Figure 4a shows that the S@NFG-5 electrode delivered a smaller voltage hysteresis of 0.19 V at 0.2 C compared with S@NFG-1 (0.23 V) and S@NFG-30 (0.3 V), respectively, with the fastest Li–S reaction kinetics being observed for NFG-5. Figure 4b shows the cycling performance of the NiFeLDH/rGO cathodes with S loading of 2 mg cm^{-2} at 0.2 C. It can be seen that the S@NFG-5 electrode can deliver an excellent initial specific capacity of 1260 mAh g^{-1} at 0.1 C and retains the capacity of 930 mAh g^{-1} at 0.2 C after 100 cycles with coulombic efficiency (CE) over 99%. In contrast, the pure sulfur, S@NFG-30, and S@NFG-1 presented much lower capacities of 236, 634, and 705 mAh g^{-1} , respectively, after 100 cycles (Figures S8 and 4b). We conducted one more group of experiments on the cycling performance of S@NFG-5 based on the conventional aluminum foil current collector (Figure S9). The electrode delivered a low capacity of 574 mAh g^{-1} after 100 cycles, notably lower than that of the carbon paper-based electrodes at 0.2 C. This result can be ascribed to the pore structure and higher pore volume of the carbon cloth-based current collector than that of the Al-based current collector. The presence of a three-dimensional pore system enhanced the electrolyte impregnation of the electrode, speeding up the kinetics between the lithium and sulfur. Figure 4c shows the rate performance of S@NFG-5 at different current densities. The discharge capacities of S@NFG-5 reached 948 mAh g^{-1} , 800 mAh g^{-1} , 728 mAh g^{-1} , and 556 mAh g^{-1} at 0.2 C, 0.5 C, 1 C, and 2 C, respectively, which were higher than those observed in the control groups, demonstrating the best rate capability of S@NFG-5. The potential activation process was responsible for the phenomenon of the growth in capacity. Charge/discharge cycling raised the electrode/electrolyte interface via enhancing electrolyte wettability, which raised the specific capacitance. After 400 cycles at 1 C, the S@NFG-5 cathode maintained a discharge capacity of 554 mAh g^{-1} and Coulombic efficiency of ~98% with S mass loading of 1.5 mg cm^{-2} (Figure 4d) and maintained a discharge capacity of 441 mAh g^{-1} with S mass loading of 2 mg cm^{-2} (Figure S10). The superior electrochemical performance indicated the superb electrocatalytic activity of NFG-5 in working Li–S batteries. The enhanced catalytic effect of NFG-5 can inhibit the shuttle effect and enhance the S utilization in lithium–sulfur (Li–S) redox chemistry.

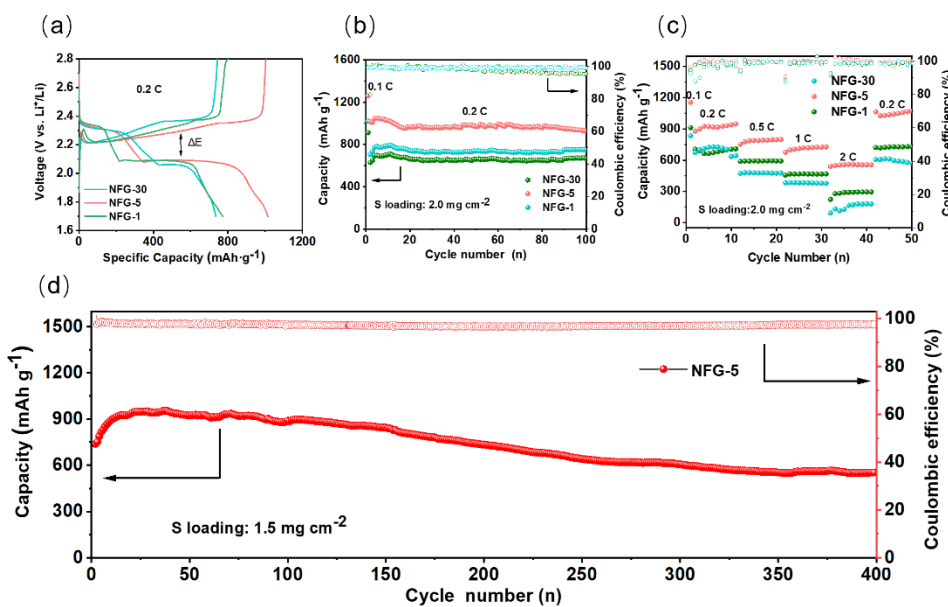


Figure 4. Electrochemical performance of NiFeLDH/rGO cathodes. (a) Discharge–charge profiles, (b) cycling performance at 0.2 C, and (c) rate capabilities of S@NFG-1, S@NFG-5, and S@NFG-30, respectively. (d) Cycling performance of S@NFG-5 electrode with S areal mass loading of 1.5 mg cm^{-2} .

4. Conclusions

In summary, S@NiFeLDH/rGO was successfully prepared as a promising host material for an Li–S battery. The assembly of NiFeLDH with rGO significantly improves the electrochemical steps of sulfur reduction. The obtained S@NiFeLDH/rGO cathode could deliver a high discharge capacity of 1014 mAh g^{-1} at 0.2 C and maintain a high capacity of 930 mAh g^{-1} after 100 cycles. In this work, our experimental findings, which are based on the electrochemical performance and fundamental knowledge developed, can help designers to create more advanced hosts for the creation of high-performance Li–S batteries and can be linked into other multi-electron chemistry energy storage technologies.

Supplementary Materials: The following supporting information can be downloaded at: <https://www.mdpi.com/article/10.3390/batteries810200/s1>, Figure S1: TGA curves of pure LDH and RGO; Figure S2: High-resolution (a) Ni 2p, (b) Fe 2p, and (c) C 1s XPS spectra of NFG-30, respectively. High-resolution (d) Ni 2p, (e) Fe 2p, and (f) C 1s XPS spectra of NFG-1, respectively; Figure S3: TEM images of (a) NFG-30, (b) NFG-5, and (c) NFG-1, respectively; Figure S4: N_2 absorption/desorption isotherms of NFG-5 and S@NFG-5; Figure S5: Chronoamperograms of Li_2S deposition of (a) NFG-1, (b) NFG-5, and (c) NFG-30, respectively; Figure S6: LSV curves of (a) NFG-1, (b) NFG-5, and (c) NFG-30, respectively; Figure S7: Koutecky–Levich plots of NFG-1, NFG-5, and NFG-30; Figure S8: Cycling performance at 0.2 C of pure sulfur; Figure S9: Cycling performance at 0.2 C of NFG-5 coated on aluminum foil; Figure S10: Cycling performance of S@NFG-5 electrode with S areal mass loading of 2 mg cm^{-2} .

Author Contributions: Conceptualization, J.X. and R.T.; methodology, J.X.; software, D.Z. and T.Z.; validation, X.K., S.J. and H.J.; formal analysis, J.X.; investigation, R.T.; resources, H.J.; data curation, S.X.; writing—original draft preparation, R.T.; writing—review and editing, S.J. and J.X.; visualization, M.L.; supervision, S.J., X.K. and H.J.; project administration, J.X.; funding acquisition, X.K. All authors have read and agreed to the published version of the manuscript.

Funding: Xianghua Kong appreciates the funding support from the Natural Science Foundation of China (21503064). Song Jin appreciates the Natural Science Foundation of China (51901104) and the Fundamental Research Funds for the Central Universities (WK2060000026).

Data Availability Statement: The data presented in this study are available on request from the corresponding author. The data are not publicly available due to confidentiality.

Conflicts of Interest: The authors declare no conflict of interest.

References

- Yin, Y.X.; Xin, S.; Guo, Y.G.; Wan, L.J. Lithium-sulfur batteries: Electrochemistry, materials, and prospects. *Angew. Chem. Int. Ed.* **2013**, *52*, 13186–13200. [[CrossRef](#)] [[PubMed](#)]
- Zhao, M.; Li, X.Y.; Chen, X.; Li, B.Q.; Kaskel, S.; Zhang, Q.; Huang, J.Q. Promoting the sulfur redox kinetics by mixed organodiselenides in high-energy-density lithium–sulfur batteries. *eScience* **2021**, *1*, 44–52. [[CrossRef](#)]
- Yue, X.Y.; Zhang, J.; Bao, J.; Bai, Y.F.; Li, X.L.; Yang, S.Y.; Fu, Z.W.; Wang, Z.H.; Zhou, Y.N. Sputtered MoN nanolayer as a multifunctional polysulfide catalyst for high-performance lithium–sulfur batteries. *eScience* **2022**, *2*, 329–338. [[CrossRef](#)]
- Manthiram, A.; F, Y.Z.; Su, Y.S. Challenges and prospects of lithium–sulfur batteries. *Acc. Chem. Res.* **2012**, *46*, 1125–1134. [[CrossRef](#)] [[PubMed](#)]
- Chen, M.; Zhao, X.; Li, Y.; Zeng, P.; Liu, H.; Yu, H.; Wu, M.; Li, Z.; Shao, D.; Miao, C.; et al. Kinetically elevated redox conversion of polysulfides of lithium–sulfur battery using a separator modified with transition metals coordinated g-C₃N₄ with carbon-conjugated. *Chem. Eng. J.* **2020**, *385*, 1385–8947. [[CrossRef](#)]
- Cheng, C.S.; Chung, S.-H. Nickel-plated sulfur nanocomposites for electrochemically stable high-loading sulfur cathodes in a lean-electrolyte lithium–sulfur cell. *Chem. Eng. J.* **2022**, *429*, 132257. [[CrossRef](#)]
- Cheng, C.S.; Chung, S.H. Rational Design of High-Performance Nickel-Sulfur Nanocomposites by the Electroless Plating Method for Electrochemical Lithium-Sulfur Battery Cathodes. *Batter. Supercaps* **2022**, *5*, e202100323. [[CrossRef](#)]
- Zhao, Y.; Wu, W.; Li, J.; Xu, Z.; Guan, L. Encapsulating MWNTs into hollow porous carbon nanotubes: A tube-in-tube carbon nanostructure for high-performance lithium–sulfur batteries. *Adv. Mater.* **2014**, *26*, 5113–5118. [[CrossRef](#)]
- Guo, Y.; Zhao, G.; Wu, N.; Zhang, Y.; Xiang, M.; Wang, B.; Liu, H.; Wu, H. Efficient synthesis of graphene nanoscrolls for fabricating sulfur-loaded cathode and flexible hybrid interlayer toward high-performance Li-S batteries. *ACS Appl. Mater. Interfaces* **2016**, *8*, 34185–34193. [[CrossRef](#)]
- Gao, T.T.; Zhou, Z.; Yu, J.Y.; Zhao, J.; Wang, G.L.; Cao, D.X.; Ding, B.; Li, Y.J. 3D printing of tunable energy storage devices with both high areal and volumetric energy densities. *Adv. Energy Mater.* **2019**, *9*, 10. [[CrossRef](#)]
- Wu, F.; Li, J.; Su, Y.; Wang, J.; Yang, W.; Li, N.; Chen, L.; Chen, S.; Chen, R.; Bao, L. Layer-by-layer assembled architecture of polyelectrolyte multilayers and graphene sheets on hollow carbon spheres/sulfur composite for high-performance lithium–sulfur batteries. *Nano Lett.* **2016**, *16*, 5488–5494. [[CrossRef](#)] [[PubMed](#)]
- Ji, X.; Lee, K.T.; Nazar, L.F. A highly ordered nanostructured carbon-sulphur cathode for lithium–sulphur batteries. *Nat. Mater.* **2009**, *8*, 500–506. [[CrossRef](#)] [[PubMed](#)]
- Zhou, G.M.; Y, L.C.; Wang, D.W.; Li, L.; P, S.F.; Gentle, I.R.; Li, F.; Cheng, H.M. Fibrous hybrid of graphene and sulfur nanocrystals for high-performance lithium–sulfur batteries. *ACS Nano* **2013**, *7*, 5367–5375. [[CrossRef](#)]
- Jin, S.; Xin, S.; Wang, L.; Du, Z.; Cao, L.; Chen, J.; Kong, X.; Gong, M.; Lu, J.; Zhu, Y.; et al. Covalently connected carbon nanostructures for current collectors in both the cathode and anode of Li-S batteries. *Adv. Mater.* **2016**, *28*, 9094–9102. [[CrossRef](#)]
- Wu, F.; Zhao, E.; Gordon, D.; Xiao, Y.; Hu, C.; Yushin, G. Infiltrated porous polymer sheets as free-standing flexible lithium–sulfur battery electrodes. *Adv. Mater.* **2016**, *28*, 6365–6371. [[CrossRef](#)]
- Su, D.; Cortie, M.; Wang, G. Fabrication of N-doped graphene–carbon nanotube hybrids from prussian blue for lithium–sulfur batteries. *Adv. Energy Mater.* **2016**, *7*, 1602014. [[CrossRef](#)]
- Laverde, J.; Rosero-Navarro, N.C.; Miura, A.; Buitrago-Sierra, R.; Tadanaga, K.; López, D. Impact of Sulfur Infiltration Time and Its Content in an N-doped Mesoporous Carbon for Application in Li-S Batteries. *Batteries* **2022**, *8*, 58. [[CrossRef](#)]
- Wang, Z.; Dong, Y.; Li, H.; Zhao, Z.; Wu, H.B.; Hao, C.; Liu, S.; Qiu, J.; Lou, X.W. Enhancing lithium–sulphur battery performance by strongly binding the discharge products on amino-functionalized reduced graphene oxide. *Nat. Commun.* **2014**, *5*, 5002. [[CrossRef](#)]
- Yao, H.; Zheng, G.; Hsu, P.C.; Kong, D.; Cha, J.J.; Li, W.; Seh, Z.W.; McDowell, M.T.; Yan, K.; Liang, Z.; et al. Improving lithium–sulphur batteries through spatial control of sulphur species deposition on a hybrid electrode surface. *Nat. Commun.* **2014**, *5*, 3943. [[CrossRef](#)]
- Hu, G.; Sun, Z.; Shi, C.; Fang, R.; Chen, J.; Hou, P.; Liu, C.; Cheng, H.M.; Li, F. A sulfur-rich copolymer@CNT hybrid cathode with dual-confinement of polysulfides for high-performance lithium-sulfur batteries. *Adv. Mater.* **2017**, *29*, 1603835. [[CrossRef](#)]
- Xu, R.; Lu, J.; Amine, K. Progress in mechanistic understanding and characterization techniques of Li-S batteries. *Adv. Energy Mater.* **2015**, *5*, 1500408. [[CrossRef](#)]
- Peng, L.; Wei, Z.; Wan, C.; Li, J.; Chen, Z.; Zhu, D.; Baumann, D.; Liu, H.; Allen, C.S.; Xu, X.; et al. A fundamental look at electrocatalytic sulfur reduction reaction. *Nat. Catal.* **2020**, *3*, 762–770. [[CrossRef](#)]
- Pang, Q.; Kundu, D.; Cuisinier, M.; Nazar, L.F. Surface-enhanced redox chemistry of polysulphides on a metallic and polar host for lithium–sulphur batteries. *Nat. Commun.* **2014**, *5*, 4759. [[CrossRef](#)] [[PubMed](#)]
- Al Salem, H.; Babu, G.; Rao, C.V.; Arava, L.M. Electrocatalytic polysulfide traps for controlling redox shuttle process of Li-S batteries. *J. Am. Chem. Soc.* **2015**, *137*, 11542–11545. [[CrossRef](#)] [[PubMed](#)]
- Marangon, V.; Scaduti, E.; Vinci, V.F.; Hassoun, J. Scalable Composites Benefiting from Transition-Metal Oxides as Cathode Materials for Efficient Lithium-Sulfur Batteries. *ChemElectroChem* **2022**, *9*, e202200374. [[CrossRef](#)]

26. Liang, X.; Hart, C.; Pang, Q.; Garsuch, A.; Weiss, T.; Nazar, L.F. A highly efficient polysulfide mediator for lithium-sulfur batteries. *Nat. Commun.* **2015**, *6*, 5682. [[CrossRef](#)]
27. Chen, M.; Xu, W.; Jamil, S.; Jiang, S.; Huang, C.; Wang, X.; Wang, Y.; Shu, H.; Xiang, K.; Zeng, P. Multifunctional heterostructures for polysulfide suppression in high-performance Lithium-Sulfur cathode. *Small* **2018**, *14*, 1803134. [[CrossRef](#)]
28. Li, M.C.; Liu, Z.; Tan, L.; Zhou, Q.Y.; Zhang, J.J.; Hou, P.P.; Jin, X.J.; Lv, T.B.; Zhao, Z.Q.; Zeng, Z.; et al. Fabrication of Cubic and Porous Carbon Cages with In-Situ-Grown Carbon Nanotube Networks and Cobalt Phosphide for High-Capacity and Stable Lithium–Sulfur Batteries. *ACS Sustain. Chem. Eng.* **2022**, *10*, 10223–10233. [[CrossRef](#)]
29. Zhang, D.; Luo, Y.; Liu, J.; Dong, Y.; Xiang, C.; Zhao, C.; Shu, H.; Hou, J.; Wang, X.; Chen, M. ZnFe₂O₄-Ni₅P₄ mott-schottky heterojunctions to promote kinetics for advanced Li-S batteries. *ACS Appl. Mater. Interfaces* **2022**, *14*, 23546–23557. [[CrossRef](#)]
30. Du, Z.; Chen, X.; Hu, W.; Chuang, C.; Xie, S.; Hu, A.; Yan, W.; Kong, X.; Wu, X.; Ji, H.; et al. Cobalt in nitrogen-doped graphene as single-atom catalyst for high-sulfur content lithium-sulfur batteries. *J. Am. Chem. Soc.* **2019**, *141*, 3977–3985. [[CrossRef](#)]
31. Adan-Mas, A.; Arévalo-Cid, P.; Moura e Silva, T.; Crespo, J.; Montemor, M.d.F. From Bench-Scale to Prototype: Case Study on a Nickel Hydroxide—Activated Carbon Hybrid Energy Storage Device. *Batteries* **2019**, *5*, 65. [[CrossRef](#)]
32. Feng, X.; Jiao, Q.; Chen, W.; Dang, Y.; Dai, Z.; Suib, S.L.; Zhang, J.; Zhao, Y.; Li, H.; Feng, C. Cactus-like NiCo₂S₄@NiFe LDH hollow spheres as an effective oxygen bifunctional electrocatalyst in alkaline solution. *Appl. Catal. B* **2021**, *286*, 119869. [[CrossRef](#)]
33. Bodhankar, P.M.; Sarawade, P.B.; Singh, G.; Vinu, A.; Dhawale, D.S. Recent advances in highly active nanostructured NiFe LDH catalyst for electrochemical water splitting. *J. Mater. Chem. A* **2021**, *9*, 3180–3208. [[CrossRef](#)]
34. Yang, M.; Sun, J.; Qin, Y.; Yang, H.; Zhang, S.; Liu, X.; Luo, J. Hollow CoFe-layered double hydroxide polyhedrons for highly efficient CO₂ electrolysis. *Sci. China Mater.* **2021**, *65*, 536–542. [[CrossRef](#)]
35. Zhang, J.; Li, Z.; Chen, Y.; Gao, S.; Lou, X.W.D. Nickel-Iron Layered Double Hydroxide Hollow Polyhedrons as a Superior Sulfur Host for Lithium-Sulfur Batteries. *Angew. Chem. Int. Ed.* **2018**, *57*, 10944–10948. [[CrossRef](#)]
36. Zhang, J.; Hu, H.; Li, Z.; Lou, X.W. Double-Shelled Nanocages with Cobalt Hydroxide Inner Shell and Layered Double Hydroxides Outer Shell as High-Efficiency Polysulfide Mediator for Lithium-Sulfur Batteries. *Angew. Chem. Int. Ed.* **2016**, *55*, 3982–3986. [[CrossRef](#)]
37. Lan, F.; Zhang, H.; Fan, J.; Xu, Q.; Li, H.; Min, Y. Electrospun Polymer Nanofibers with TiO₂@NiCo-LDH as Efficient Polysulfide Barriers for Wide-Temperature-Range Li-S Batteries. *ACS Appl. Mater. Interfaces* **2021**, *13*, 2734–2744. [[CrossRef](#)]
38. Zubair, M.; Daud, M.; McKay, G.; Shehzad, F.; Al-Harthi, M.A. Recent progress in layered double hydroxides (LDH)-containing hybrids as adsorbents for water remediation. *Appl. Clay Sci.* **2017**, *143*, 279–292. [[CrossRef](#)]
39. Chen, G.; Wang, T.; Zhang, J.; Liu, P.; Sun, H.; Zhuang, X.; Chen, M.; Feng, X. Accelerated hydrogen evolution kinetics on NiFe-layered double hydroxide electrocatalysts by tailoring water dissociation active sites. *Adv. Mater.* **2018**, *30*, 1706279. [[CrossRef](#)]
40. Ananthraj, S.; Karthick, K.; Venkatesh, M.; Simha, T.V.S.V.; Salunke, A.S.; Ma, L.; Liang, H.; Kundu, S. Enhancing electrocatalytic total water splitting at few layer Pt-NiFe layered double hydroxide interfaces. *Nano Energy* **2017**, *39*, 30–43. [[CrossRef](#)]
41. Xie, S.; Chen, X.; Wang, C.; Lu, Y.R.; Chan, T.S.; Chuang, C.H.; Zhang, J.; Yan, W.; Jin, S.; Jin, H.; et al. Role of the Metal Atom in a Carbon-Based Single-Atom Electrocatalyst for Li-S Redox Reactions. *Small* **2022**, *18*, 2200395. [[CrossRef](#)] [[PubMed](#)]